



## Effects of microporosity on the elasticity and yielding of thin-walled metallic hollow spheres



Jinliang Song<sup>a,b</sup>, Quansheng Sun<sup>a</sup>, Zhenning Yang<sup>b</sup>, Shengmin Luo<sup>b</sup>, Xianghui Xiao<sup>c</sup>, Sanjay R. Arwade<sup>b</sup>, Guoping Zhang<sup>b,\*</sup>

<sup>a</sup> Department of Civil Engineering, Northeast Forestry University, Harbin 150040, China

<sup>b</sup> Department of Civil and Environmental Engineering, University of Massachusetts Amherst, Amherst, MA 01003, USA

<sup>c</sup> Advanced Photon Source, Argonne National Laboratory, Argonne, IL 60439, USA

### ARTICLE INFO

#### Keywords:

Ferrous alloys  
Finite element method  
Mechanical characterization  
Nanoindentation  
Porous materials  
Tomography

### ABSTRACT

Knowledge of the mechanical properties of porous metallic hollow spheres (MHS) thin wall is of key importance for understanding the engineering performance of both individual ultralight MHS and the innovative MHS-based bulk foams. This paper presents the first integrated experimental and numerical study to determine the elasticity and yielding of the porous MHS wall and their dependence on its microporosity. Nanoindentation was used to probe the Young's modulus and hardness of the nonporous MHS wall material, and synchrotron X-ray computed tomography (XCT) conducted to obtain its porous microstructure and pore morphology. Three-dimensional finite element modeling was performed to obtain the mechanical response of microcubes with varying porosity trimmed from the XCT-derived real digital model of the porous MHS wall. Results show that both the Young's modulus and yield strength of the porous wall decrease nonlinearly with increasing porosity, and their relationships follow the same format of a power law function and agree well with prior experimental results. The empirical relations also reflect certain features of pore morphology, such as pore connectivity and shape. These findings can shed lights on the design, manufacturing, and modeling of individual MHS and MHS-based foams.

### 1. Introduction

Metallic hollow sphere (MHS)-based materials, a kind of innovative, high-performance cellular foams, are made of ultralight, thin-walled MHS. The advantageous mechanical properties of MHS-based foams include, for example, very low density, high specific strength (i.e., strength to mass ratio), and very high energy-absorbing capability. They are widely used or have the great potential for being used in many functional structures such as car bumpers, automotive structural components, biomedical artificial limbs, ballistic armors, sound barriers, and damping devices, among others [1]. With latest metallurgical technologies, the characteristics of individual MHS such as the diameter and wall thickness can be finely tuned, and an assemblage of MHS can be bonded together by sintering, soldering, or epoxy resin to form different structural configurations and arrangements (e.g., simple cubic, body-centered cubic, face-centered cubic packing, hexagonal-closed packing, and completely random packing). To understand the mechanical performance of the MHS-based foams, prior experimental investigations commonly focused on the compressive,

tensile, fatigue, and dynamic behavior [2–5]. In addition, a few studies were conducted to model their mechanical properties, and such numerical modeling typically dealt with the mechanical behavior at large plastic deformation as well as their energy-absorbing capacity [6,7]. These work concluded that a better prediction of the mechanical properties of MHS-based materials and structures could be obtained if the microstructure (e.g., porosity and pore size) and properties of the MHS wall material itself are clearly known. In this regard, Caty et al. conducted X-ray computed tomography (XCT) to characterize the microstructure of a MHS-based foam material, and used the real microstructure obtained by XCT as the input model for finite element modeling (FEM). This method's significant advantage was the use of a physically realistic digital model that reflected the real morphology and microstructure of the porous MHS-based foam, instead of idealized, assumed, or sometimes over-simplified microstructure models [8]. Furthermore, Shufrin et al. [9] proposed a simplified continuum model for a hollow-sphere assembly using the Cosserat's three-dimensional (3D) continuum theory to describe the negative Poisson's ratio of MHS-based materials subject to small strains where various regular config-

\* Corresponding author.

E-mail addresses: [zhangg@umass.edu](mailto:zhangg@umass.edu), [gzhang@alum.mit.edu](mailto:gzhang@alum.mit.edu) (G. Zhang).

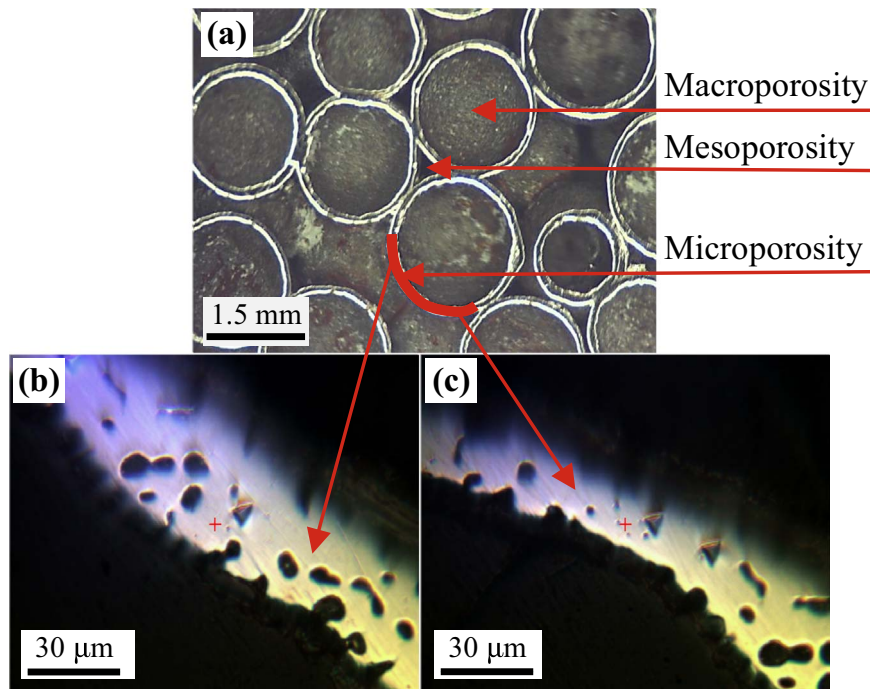


**Fig. 1.** Three different types of porosities in MHS-based foam materials: (a) a cross-section showing three kinds of pores at different scales; (b) and (c) cross-sections of the porous thin wall showing micropores.

urations of spheres were considered [9].

Generally MHS-based materials have distinctly high energy-absorbing capability due to their ultrahigh porosity, and hence accurate control of porosity plays an important role in tuning their mechanical performance. Normally, three different types of porosities at different scales exist in most MHS-based materials (Fig. 1): macroporosity, mesoporosity, and microporosity [10]. Macroporosity is the large central pore inside each MHS, which is mainly influenced by the diameter and wall thickness; Mesoporosity refers to the void space among spheres, and their different packing configurations result in variable mesoporosity; The void fraction within the porous thin wall of the MHS makes up the microporosity. In fact, besides the solid material itself and bonding types of MHS-based foams, most prior studies focused on the mode of MHS arrangement and size of individual spheres, which are mainly related to mesoporosity and macroporosity, respectively. To date, it appears that the effects of microporosity on the performance of MHS-based materials have received little attention, despite the fact that most of these materials consist of hollow spheres with porous thin walls. Apparently, an excessively high microporosity can degrade the mechanical properties such as elastic modulus and yield strength of the porous thin wall that makes up the MHS. On the other hand, a too low microporosity increases its density and load capacity, but decreases the energy-absorbing capacity, making the MHS-based foams less attractive as a unique functional material. Therefore, it is of significant importance to understand how microporosity affects the mechanical properties of the porous thin wall, particularly based on its real physical microstructure and pore characteristics.

For porous materials, several approaches have been developed concerning the relationship between the mechanical property and porosity. Many formulae were proposed based on the micromechanics method [11–13] and minimum solid area (MSA) method [14,15]. Most of these formulations are semi-empirical in nature since the real microstructure corresponding to a particular formula is not precisely known. In addition, they may unlikely provide powerful predictions for the porous wall with nonuniform pore sizes and irregular pore shapes, the two typical parameters accounting for the geometrical nature of porosity. For example, Roberts and Garboczi used FEM to study the

influence of porosity and pore shape on the elastic properties of some porous ceramics, and established three types of models to find the dependence of elastic modulus and Poisson's ratio on porosity: overlapping solid spheres, overlapping spherical pores, and overlapping ellipsoidal pores [16]. Other FEM simulation work [17,18] also considered hard (such as carbide precipitates) or soft (such as cracks) inclusions in a uniform matrix, which may provide guidance on modeling materials with pores (i.e., same as soft inclusions). Although most of the pores in the considered materials are spherical or oval, irregular polygonal pores also exist in the randomly configured microstructure. Such results are certainly very useful, but they all suffer from the limitation that one deals with errors from both theoretical approximations and incongruence between the real microstructure and idealized pore models. Therefore, it is more rational to obtain and use the real pore geometry (e.g., size, shape), spatial distribution (e.g., spacing), and pore connectivity (e.g., closed vs. open pores) for the modeling of these porous materials.

Although the porous nature of the MHS thin wall has been recognized, little effort has been made to study the mechanical properties of the porous wall material itself, probably owing to partly the shell-like shape of the thin wall and partly the relatively small size of the MHS. This paper presents the first effort that integrates experimentation and FEM simulation to investigate the elasticity and yielding of the porous MHS thin wall and their dependence on its microporosity. Experimental work consisted of nanoindentation and high-energy synchrotron XCT, while FEM simulation was performed on selected, three-dimensional (3D) porous microcubes of varying porosity extracted from the XCT-derived digital model of the MHS thin wall. Simulation results are then used to derive the relationships linking Young's modulus and yield strength with porosity. These findings can expectedly advance the design and manufacturing of individual MHS and MHS-based materials as well as the modeling and prediction of their mechanical performance.

## 2. Materials and methods

### 2.1. Materials

The studied MHS, acquired from Fraunhofer Institute for Advanced Materials (IFAM) (Dresden, Germany), were made of ferrous alloys whose mechanical properties are not exactly known. The size of the MHS varied slightly with a range of 2–3 mm in diameter, and the wall is highly porous and has a variable thickness of approximately 0.01–0.04 mm (Fig. 1b and c). Careful observation of the wall cross-section under an optical microscope revealed that the morphology of pores on the wall is highly irregular in shape and is hardly discernible distinctly at low magnifications. Most MHS are different, and each MHS has its own diameter, wall thickness, and porosity. Careful measurements showed that the bulk density of individual MHS ranges from 0.40 to 0.63 g/cm<sup>3</sup>. As discussed later, the approximate microporosity of the MHS wall ranged from ~5% in local sections to as high as ~42% for an entire cross-sectional surface.

To prepare the cross-sectional surface of the MHS wall for nanoindentation testing, a whole single MHS was first embedded in a fast-curing Samplkwick acrylic (Buehler Inc., Illinois, USA) to facilitate subsequent polishing. Owing to its lightweight, a MHS tended to float on the surface of the liquid acrylic before it hardened. Therefore, a two-stage embedment method was adopted. In the first stage, the MHS was only partially embedded in the hardened acrylic owing to its floating. In the second stage, more liquid acrylic was added to the surface of the hardened acrylic and the previously partially embedded MHS then became fully submerged and embedded inside the acrylic. Since the MHS was stuck to the hardened acrylic, it would not become floated on the liquid acrylic during the second stage. Upon complete hardening (e.g., at least 1 h), the cured acrylic sample was removed from the mold, and then progressively polished in a MetaServ 250 polisher (Buehler Inc., Illinois, USA) with sandpapers of increasing grain fineness (i.e., from # P180 to # P4000), and the final polishing was achieved by 0.03 μm alumina suspension (Fig. 2a and b). The final polished surface was further cleaned with filtered pressurized air and alcohol to remove residual polishing dust prior to accepting indentation.

Energy-dispersive X-ray spectroscopy (EDXS) was also performed on a single MHS to analyze its chemical composition in an FEI Magellan 400 XHR scanning electron microscope (SEM, FEI Inc., Hillsboro, OR, USA) with a built-in Oxford X-MAX EDXS spectrometer. The examined sphere was also roughly polished to expose its cross-sectional surface of the thin wall so that elemental composition of the thin wall's interior as well as the external surface could be obtained.

### 2.2. Nanoindentation testing

A Keysight G200 nanoindenter (Keysight Technologies, Inc., Santa Rosa, CA) equipped with a Berkovich diamond indenter tip of < 20 nm in radius was used to perform indentation tests on the MHS thin wall. To obtain the mechanical properties of the nonporous wall material, five (5) indents were made on carefully selected (under the assistance of a built-in optical microscope), nonporous locations on the polished surface, preferably near the centerline of the wall. Indentation loading employed a continuous stiffness measurement (CSM) module with a constant indentation strain rate ( $\dot{h}/h$ ) of 0.05 1/s to a maximum depth of 2000 nm. A duration of 10 s for holding load constant was allowed at the maximum load to eliminate the effect of creep on the initial slope of the elastic unloading curve. Based on the recorded load-displacement curves, the Young's modulus ( $E$ ) and hardness ( $H$ ) were determined by the Oliver and Pharr [19] method.

The hardness of the material,  $H$ , is given by:

$$H = \frac{F_{\max}}{A_c} \quad (1)$$

where  $F_{\max}$  is the maximum indentation load,  $A_c$  the projected contact area between the indenter tip and sample. For an indenter tip of known geometry, this contact area is a function of the indentation depth  $h$ , which is determined by calibrating the indenter tip on standard materials (e.g., fused silica, aluminum) with known mechanical properties. The reduced modulus ( $E_r$ ) of the contacting interface is given by:

$$E_r = \frac{\sqrt{\pi}}{2\beta\sqrt{A_c}}S \quad (2)$$

where  $\beta$  is a dimensionless correction factor for indenter tip geometry, commonly taken as 1.05 for a Berkovich tip,  $S$  the contact stiffness that is determined by solving the vibration equations for the indenter-sample system owing to the use of the CSM loading method. The Young's modulus,  $E$ , can be determined by [20]:

$$\frac{1}{E_r} = \frac{1 - \nu^2}{E} + \frac{1 - \nu_i^2}{E_i} \quad (3)$$

where  $E$  and  $E_i$  are the Young's moduli of the sample and diamond tip, respectively.  $\nu$  and  $\nu_i$  are the Poisson's ratio of the sample and diamond tip, respectively. For a diamond tip,  $E_i$  and  $\nu_i$  are 1141 GPa and 0.07, respectively. For the nonporous MHS wall,  $\nu$  is assumed to be 0.3. Noteworthy is that a small variation in the assumed Poisson's ratio of the sample has negligible influence on the calculation of its Young's modulus [21]. Residual indents were also imaged by the aforementioned SEM used for chemical analysis.

### 2.3. X-ray computed tomography

X-ray computed tomography (XCT), a non-destructive technique for material characterization (which can minimize disturbance to the pore morphology and pore network of the MHS thin wall), was used to characterize the 3D porous microstructure and micromorphology of the MHS wall [22]. A single as-received (i.e., without any pre-processing to avoid disturbance to the pore morphology) MHS was directly examined by high-energy synchrotron XCT in the 2-BM-A Beamline at the Advanced Photon Source (APS), Argonne National Laboratory, using a filtered white beam from the bending magnet source. The peak energy of the beam was 60 keV, and the projection images were recorded by an X-ray microscope that is composed of a sCMOS camera (pco.edge 5.5), a 7.5× Mitutoyo long-working-distance lens, and 20 μm thick LuAG:Ce scintillator. Totally 1500 images were acquired in the rotation angle range of 0–180° with a step size of 0.12°. Tomography reconstruction was performed by the Gridrec algorithm [23] implemented in Tomopy [24].

Since the two-dimensional (2D) cross-section images obtained by XCT cannot show the 3D volumetric porosity and pore morphology, further processing was performed to reconstruct the 3D digital model of the XCT-scanned section within the individual MHS. The 2D slice images were segmented and binarized with a Python-based Scikit-image package [25]. The segmented binary images were then input to a program, Avizo (FEI Inc., Hillsboro, OR, USA), to reconstruct the 3D digital model of the scanned MHS section. The resulting slice images had an isotropic voxel size of 0.87 μm.

### 2.4. Finite element modeling

FEM simulation was conducted to analyze the mechanical properties of the porous thin wall using a commercial platform, ABAQUS v.6.10 (Dassault Systèmes Americas Corp., Waltham, MA, USA). A series of porous micrometer-sized cubes of varying porosity were trimmed from the aforementioned XCT-derived 3D digital model of the porous wall, and hence each microcube model was based on the real microstructure and pore morphology. Depending upon their locations and orientations, the microcubes had a side length of either 20 or 30 μm and were meshed in Avizo (FEI Inc., Hillsboro, OR, USA),

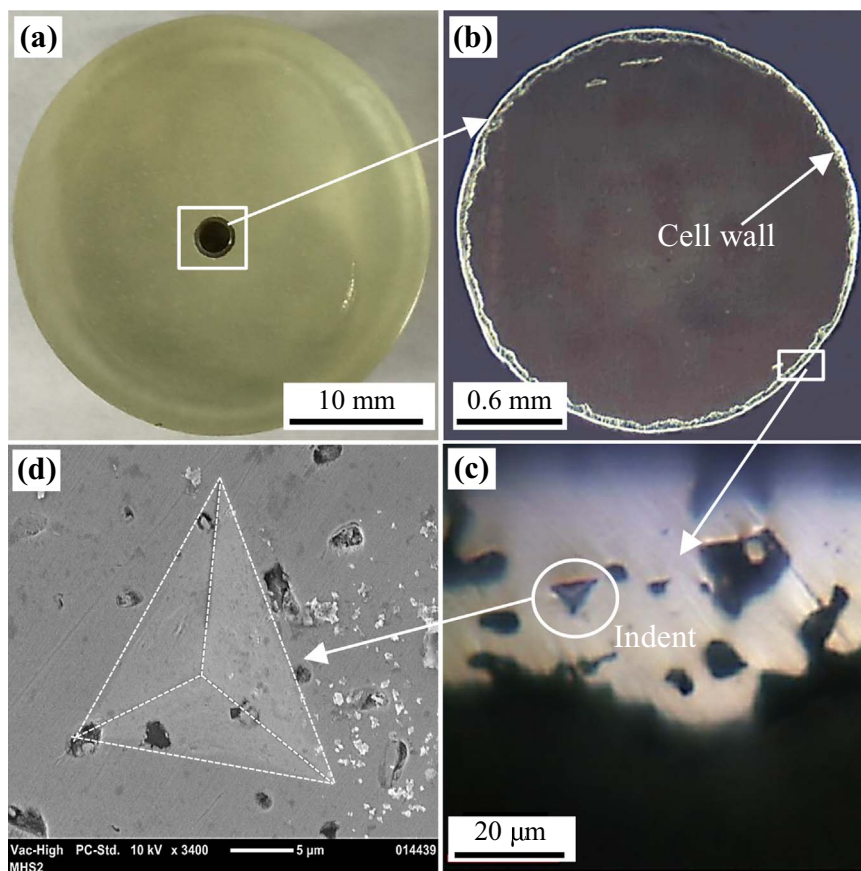


**Fig. 2.** (a) and (b) Polished MHS sample for nanoindentation testing; (c) optical micrograph showing the wall microporosity and a residual indent; and (d) a residual indent observed under a scanning electron microscope (SEM).

and their porosities were calculated directly from the 3D digital models. Each model was then imported into ABAQUS from Avizo for further FEM simulation of uniaxial compression testing using the C3D4 as the basic element type. In the simulation, a deformable microcube was placed between two rigid and smooth end platens, with the bottom one as a fixed boundary and the top one as a loading punch. All degrees of freedom were constrained for the two end platens except the vertical displacement of the top platen, so that the compression was performed along the vertical direction via a displacement-controlled mode. Because nanoindentation testing only provided its Young's modulus and hardness, the nonporous wall material was simply treated as a linearly elastic, perfectly plastic material. As such, three parameters were needed to describe its mechanical behavior: Young's modulus, initial yield strength, and Poisson's ratio. The former two were obtained from the nanoindentation testing, while the Poisson's ratio was again assumed to be 0.3. For the contact properties between the microcube and rigid platens, the tangential behavior was defined as frictionless, whereas the normal contacts were assigned as the "hard contact" algorithm. All simulations were performed under the ABAQUS standard mode to obtain the elastic response and initial yield strength of the porous microcubes of varying porosities.

### 3. Results and discussion

#### 3.1. Chemical composition of the MHS

Fig. 3 shows the EDXS spectra obtained from both the external surface and wall interior, and Table 1 summarizes the quantitative results. Clearly, except the presence of < 1.0 wt% P, which is likely an impurity introduced by polishing, the sphere surface and wall interior have nearly the same elemental composition and nearly identical

spectra. The sphere is made of nearly entire Fe (96–98 wt%), with C content ranging from 0.8 to 1.99 wt%. Again, the higher carbon content of the wall cross-section may be caused by the impurities from the embedding resin and polishing. These data suggest that the MHS material is a kind of medium carbon steel.

#### 3.2. Mechanical properties of the nonporous wall material obtained by nanoindentation

A prepared MHS specimen embedded in acrylic and a representative residual indent are shown in Fig. 2. Clearly the wall is very thin when compared with the diameter, and it is indeed highly porous. Fig. 2c and d show typical residual indents on the MHS thin wall observed by optical microscopy and SEM, respectively. Under the optical microscope, the indent appears to be made on a pore-free spot and does not interfere with the nearby pores. However, under the SEM, much smaller pores become observable, and the indent is interfered by relatively small pores. Such observation may help interpret the subsequent nanoindentation results.

Five representative indentation load-displacement curves for the nonporous wall material are shown in Fig. 4a. Apparently, the maximum forces are nearly the same (i.e., 225–250 mN) to reach the maximum indentation depth of ~2000 nm, and the material exhibits certain creep behavior, as evidenced by the continuous increase in depth during the 10 s period of holding constant load. The loading curves are slightly scattered at the depth of > 700 nm, but all the unloading curves nearly overlap with each other, indicating a consistent elastic response to unloading. As discussed below, the scattering in the loading curves may be caused by the pores within the indented zone, and some pores are too small to be discernible under the optical microscope.

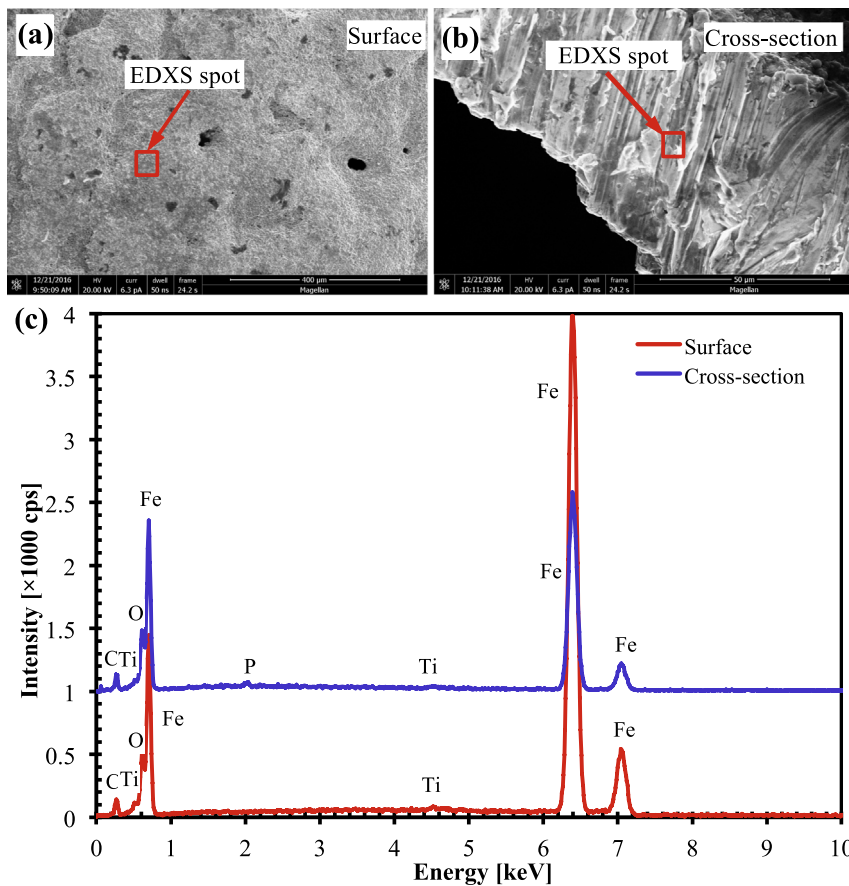


**Fig. 3.** Chemical analysis of MHS by EDXS: (a) and (b) SEM micrographs showing the EDXS-analyzed spot on external surface and wall cross-section, respectively; (c) Spectra of the analyzed spots shown in (a) and (b).

**Table 1**  
Elemental composition of the MHS obtained by EDXS.

Element	External surface		Cross-section	
	wt%	atom %	wt%	atom %
C	0.80	3.58	1.99	8.50
O	0.28	0.95	0.34	1.09
Ti	0.38	0.42	0.50	0.54
Fe	98.54	95.02	96.62	88.95
P	–	–	0.56	0.93
Total	100.00	99.99	100.01	100.01

Fig. 4b and c show the corresponding Young's modulus and hardness obtained from the five indents, respectively. At small depths (e.g.,  $h < 150$  nm), significant scattering exists for both the Young's modulus and hardness, most likely caused by the surface roughness or other surface imperfections caused by polishing. As such, data within this depth range (i.e.,  $h < 150$  nm) are not considered as representative properties. Interestingly, both the elastic modulus and hardness decrease with increasing indentation depth. In other words, they both exhibit size-dependent behavior. In fact, size-dependent elasticity has been observed in small-dimensional materials (e.g., nanowires, nanobeams) [26–28]. For the studied MHS wall material, several factors may contribute to the observed size-dependent Young's modulus: (1) it may be the intrinsic behavior of the ferrous alloy (i.e., the wall material itself) [29,30]; (2) the elastic zone caused by indentation loading is significantly greater than the observed residual indent, and such a large elastic zone may contain pores near and beneath the selected nonporous indenting spot (as discussed early, Fig. 2d); and (3) since the wall is very thin, the elastic indentation zone may readily extend into

the embedding acrylic that is much softer than the ferrous alloy. As such, the combined elastic response of the load-affected indentation zone depends upon the nonporous wall material, pores with this zone, and the softer embedding acrylic, and this becomes more pronounced with increasing indentation depth (i.e., the elastic indentation zone may easily propagate outside the thin wall owing to its very small thickness of 30–40  $\mu$ m). A detailed discussion of size-dependent elasticity is out of the scope of this work. Nevertheless, the Young's modulus at smaller indentation depth should be more representative for the nonporous wall. In this study, the values at the depth of 150 nm are considered to be the true elastic properties of the nonporous wall material. Data at depths of  $< 150$  nm are affected by surface roughness and other surface imperfections, while data at depths of  $> 150$  nm may be affected by nearby pores and the embedding acrylic. The average Young's modulus from the five indents is  $E=207 \pm 10.4$  GPa. To check the accuracy of this value, Table 2 lists the reported Young's moduli for a range of ferrous alloys obtained by both uniaxial tension and nanoindentation testing. Clearly, the value obtained in this study agrees very well with those reported in the literature. Noteworthy is that certain variation in Young's modulus reported in Table 2 is caused by the difference in the ferrous alloys' composition.

Indentation size effect is apparent in the hardness-indentation depth curves shown in Fig. 4c. Such a size effect may also result from the material's intrinsic behavior as well as the nearby pores and embedding acrylic. However, compared with the Young's modulus, hardness is much less prone to be affected by the defects nearby the indent, because the plastic zone is much smaller than the elastic zone. Therefore, with the consideration of indentation size effect, the Nix-Gao model [31] is used to obtain the macroscale hardness of the nonporous wall material:

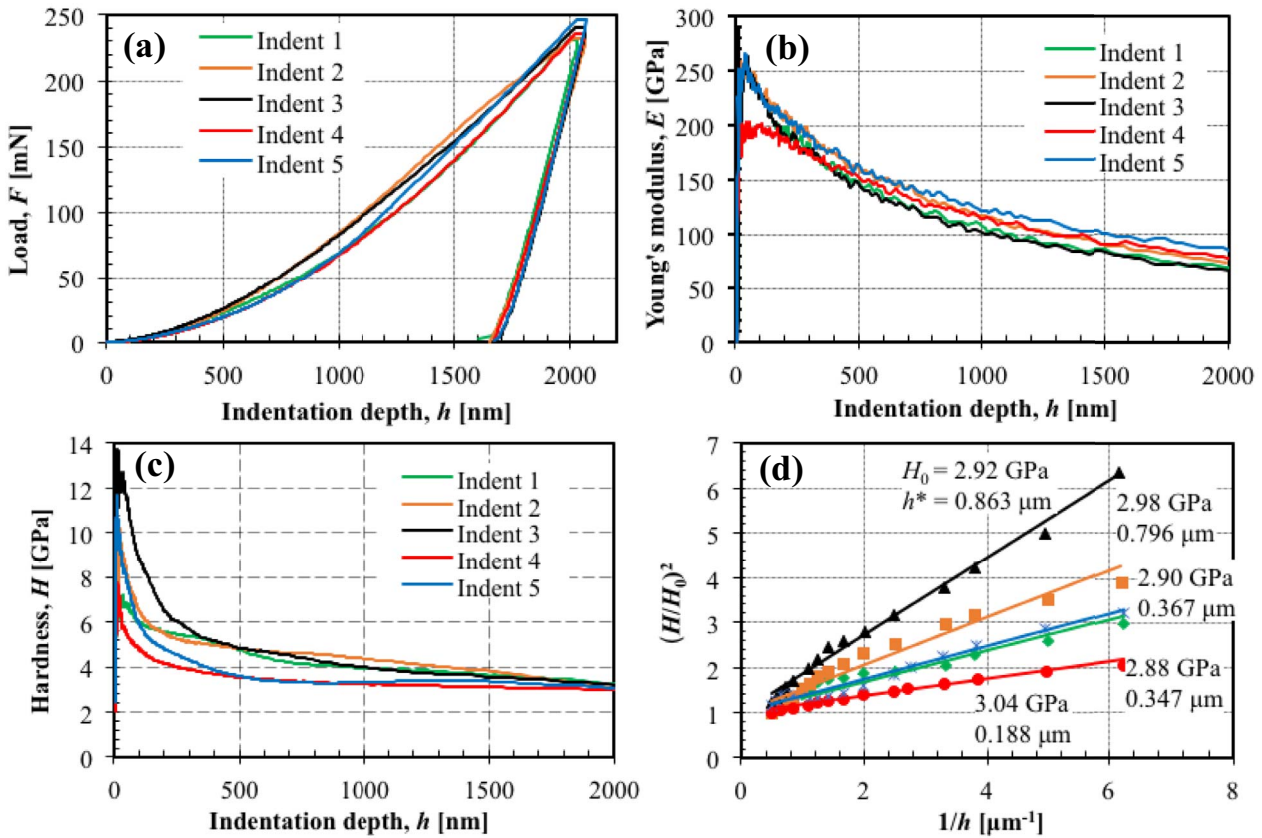


Fig. 4. Results of nanoindentation testing: (a) load-displacement curves for five indents; (b) and (c) derived Young's modulus and hardness, respectively; (d) Fitting the size-dependent hardness with the Nix-Gao model.

Table 2

Comparison of the Young's moduli and yield strengths of ferrous alloys obtained by tensile testing and nanoindentation.

Ferrous alloy	$E_t$ (GPa)	$E_n$ (GPa)	$H_n$ (GPa)	$\sigma_{Y(t)}$ (MPa)	$\sigma_{Y(n)}$ (MPa)	Reference
AISI 316L		187 ± 18	2.3 ± 0.1			Ballarre et al. [33]
DP490	205			299		Kim et al. [34]
DP980	195			1026		Cheng et al. [35]
H13		288 ± 64	6.6 ± 2.3			Kumar et al. [36]
Mild270	225			143		Kim et al. [34]
MHS wall		207 ± 10.4	2.95 ± 0.09		982	This study

$E_t$  and  $E_n$  denote the Young's moduli determined by tension and nanoindentation testing, respectively;  $H_n$  denotes the hardness obtained by nanoindentation;  $\sigma_{Y(t)}$  and  $\sigma_{Y(n)}$  denote the yield strength determined by tension and nanoindentation testing, respectively.

$$\frac{H}{H_0} = \sqrt{1 + \frac{h^*}{h}} \quad (4)$$

where  $H$  is the nanoscale hardness obtained by indentation;  $H_0$  the hardness at an infinite depth, or a macroscale hardness;  $h^*$  the characteristic length based on the tip geometry, shear modulus, and  $H_0$ . The hardness-depth data for the MHS thin wall can be fit by the Nix-Gao model, as shown in Fig. 4d. The average value of the  $H_0$  from the five indentations is 2.95 ± 0.09 GPa.

It is generally agreed that indentation hardness is essentially a measure of the plastic yield strength for most metallic materials. In fact, according to the Tabor Law [32], the yield strength  $Y_s$  can be roughly estimated from the macroscale hardness  $H_0$  via the following equation [32]:

$$H_0 \approx 3Y_s \quad (5)$$

As such, the yield strength  $Y_s$  of the nonporous ferrous alloy making up the MHS can then be taken as 982 MPa. This value is also compared in Table 2 with the yield strengths of other ferrous alloys reported in the literature [33–36], and the difference may be caused by the alloys'

compositional difference. In summary, by means of nanoindentation testing on the pore-free locations in the MHS thin wall, the Young's modulus and yield strength of the pore-free ferrous alloy are obtained, which can then be used as the essential input parameters for subsequent FEM simulation of the mechanical response of porous MHS thin wall.

### 3.3. Microstructure characterization by synchrotron XCT

Fig. 5 shows four selected synchrotron XCT micrographs for the horizontally sliced cross-sections of an individual MHS. As the horizontal cross-section moves closer to the center of the sphere, the observed “apparent” wall thickness becomes smaller, and the actual thickness (which is better reflected in Fig. 5c and d) is about 15–35 μm. Even on the same cross-section, the wall thickness varies considerably, and the sliced cross-sectional ring is not a perfect circle. The corresponding two-dimensional (2D) porosity  $\Phi$  (i.e., the ratio of the total area of the pores within the wall to the total area of the porous wall, the latter including both pores and solid metal) of each cross-section is also

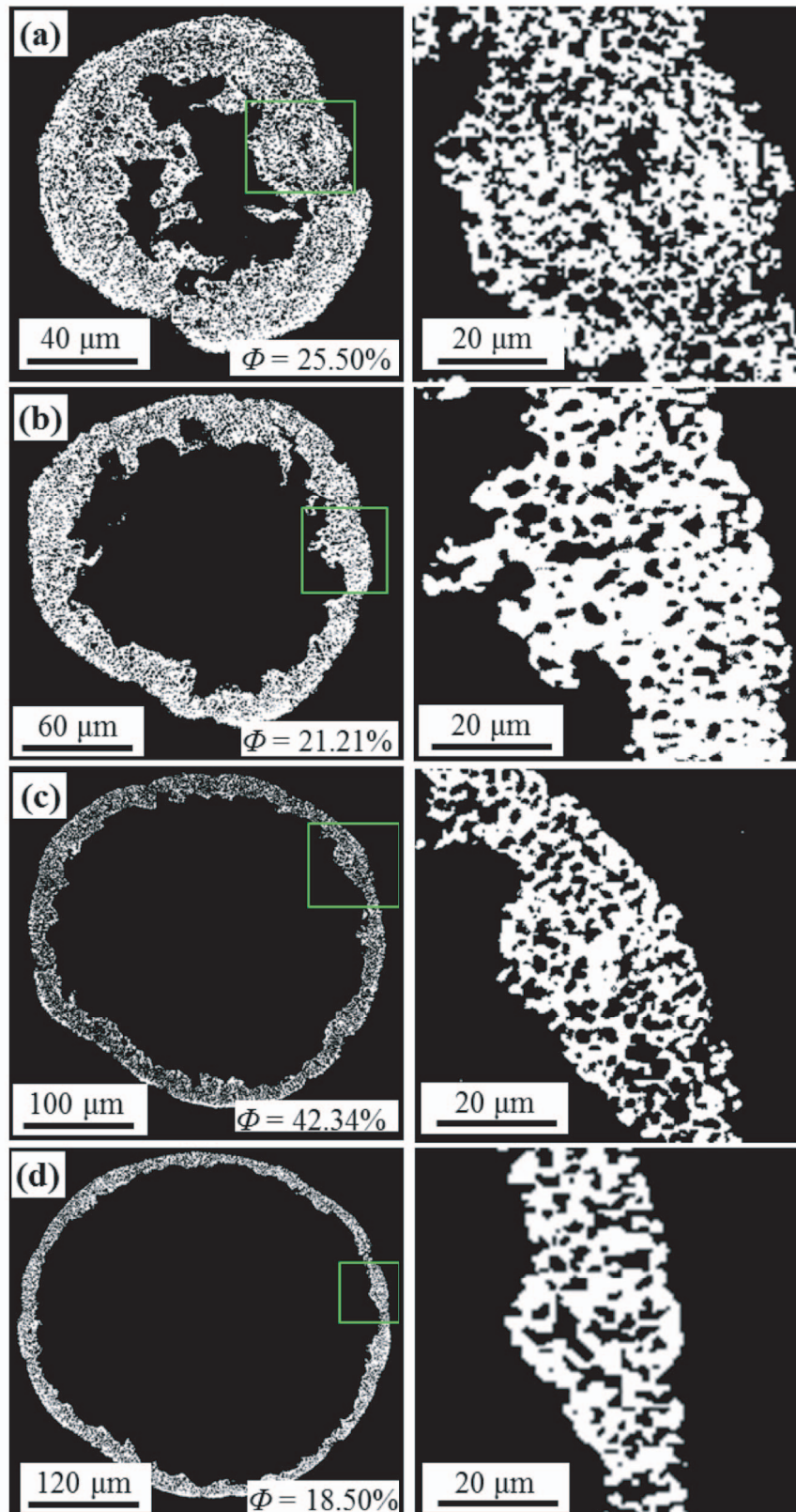


**Fig. 5.** XCT slice images showing the shape of the cross-sections and pore morphology of the MHS thin wall: images on the right column are the magnified view of a small-boxed section in the left column and same row.

shown in the micrograph. In fact, the 2D porosity from different cross-sections varies significantly and, for the four selected micrographs, ranges from 18.50% to 42.34%.

Further noteworthy is the micropore morphology, including shape, size, and interconnectivity. As seen from the zoomed view of small segments selected from each of the cross-sections (Fig. 5), the shape of

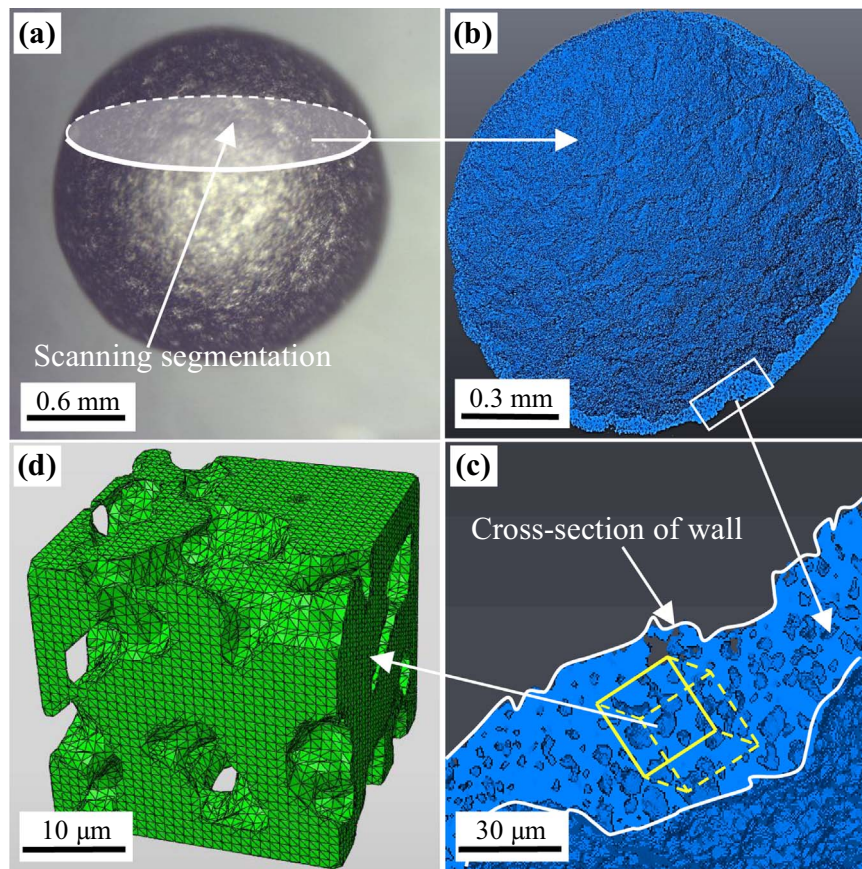


**Fig. 6.** XCT-derived 3D digital model of the porous MHS thin wall: (a) a MHS showing the scanning segmentation; (b) reconstructed 3D digital model of the entire scanned section; (c) a zoomed view of the cross-section of the thin wall; (d) a 3D microcube trimmed from the thin wall digital model.

the pores is highly irregular. Most pores are elongated, and circular pores are indeed rare. Certain small pores are interconnected or merged together to form a highly elongated, relatively large void or cavity. Moreover, most pores at both the inner and outer edges of the cross-sectional ring are not self-closed, but are open to the hollow center or to the outer space. As discussed later, these characteristics of pore morphology actually affects the elastic and yielding behavior of the porous MHS wall. Finally, the size of the pores also varies significantly and randomly. The smallest pores are in the range of a few micrometers, while the large ones can reach to 10–15 μm.

Fig. 6a and b shows the reconstructed 3D digital model of the entire section scanned by the XCT. Neither the external or internal surface of the MHS is smooth. Moreover, the internal surface has randomly distributed, irregular protrusions and hence has a much higher roughness than the external one. Fig. 6c shows the details of wall cross-section at a much higher magnification. Again, the pores are highly irregular in shape and are randomly distributed, and the size of the pores ranges from a few micrometers to 10–15 μm. Some pores are interconnected and it is hence difficult to differentiate one from the other. Such a 3D digital model allows for the detailed study of microstructure features, including the presence of inclusions, cracks, and pores, and the 3D porosity can be calculated directly from the digital model.

The complexity of the pore size and morphology makes it difficult and challenging to use artificially constructed physical models with idealized porous microstructure to simulate the porous wall's mechanical properties. Therefore, the XCT-derived 3D digital model of the MHS wall reflecting the actual microstructure and pore morphology was used to simulate via FEM its mechanical properties. Fig. 6d shows a typical microcube of 30 μm in size trimmed from a relatively thicker section of the wall. Clearly, the shape of the pores is again highly

irregular, and some pores on the surfaces of the cube are not self-closed.

### 3.4. Effect of microporosity on the properties of the MHS thin wall

To facilitate the extraction of some simple material's properties such as Young's modulus and yield strength of the porous MHS wall, a total of 14 microcubes of 20 or 30 μm in size were trimmed from the 3D digital model (Table 3), followed by fine meshing for subsequent FEM simulation. A special consideration for selectively cutting the 14 microcubes was to vary their porosities as widely as possible. In fact, the 3D volumetric porosity of these microcubes ranges from 5.41% to

**Table 3**  
Summary of the size, porosity, and simulated Young's modulus and yield strength of the MHS wall microcubes.

Sample ID	Cube dimension (μm)	$\Phi$ (%)	$E/E_s$	$Y/Y_s$
1	30	0.00	1.00	1.00
2	20	5.41	0.87	0.72
3	20	7.22	0.84	0.70
4	20	9.53	0.78	0.56
5	30	11.11	0.76	0.51
6	30	11.60	0.72	0.50
7	30	12.25	0.7	0.51
8	20	12.98	0.69	0.47
9	20	13.11	0.72	0.49
10	20	13.60	0.67	0.41
11	20	14.61	0.63	0.40
12	20	15.92	0.59	0.39
13	20	19.22	0.58	0.34
14	20	26.08	0.49	0.31
15	30	32.88	0.28	0.16

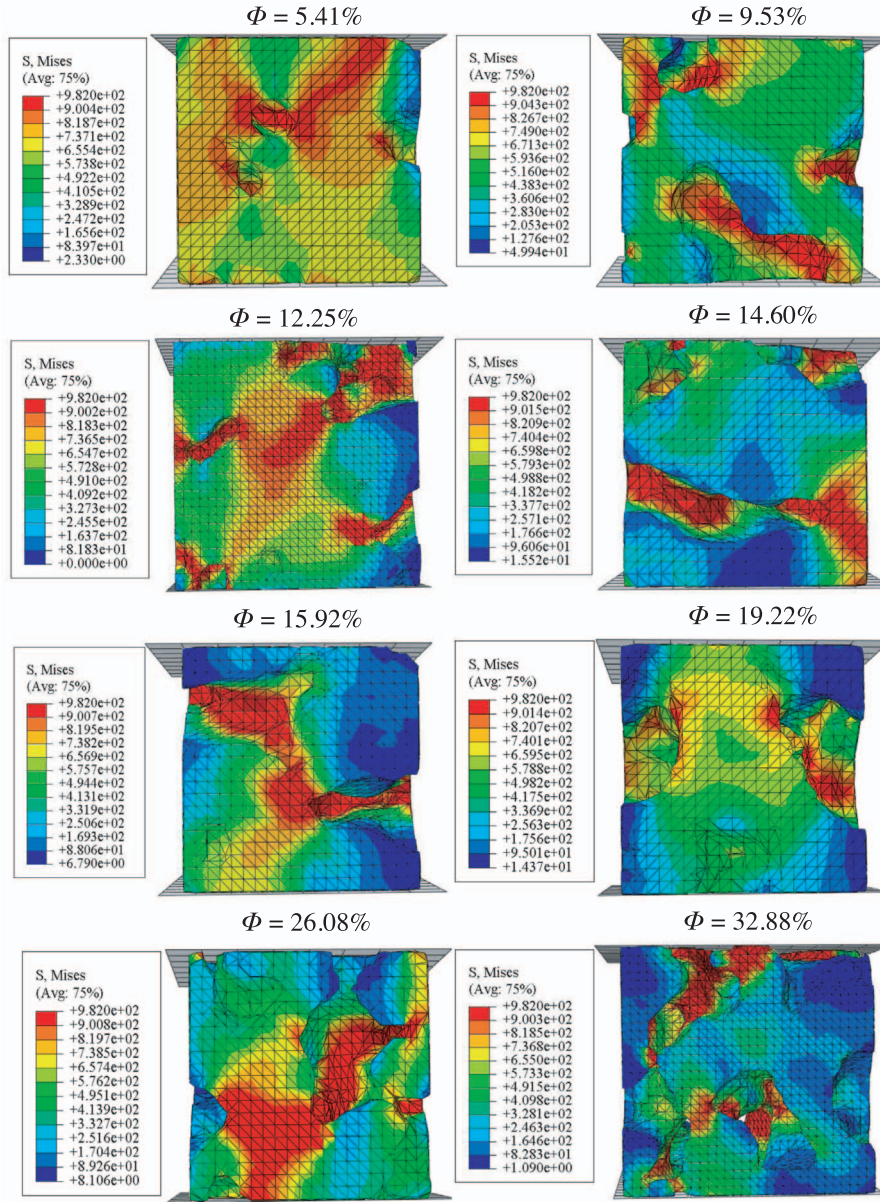


**Fig. 7.** FEM simulated von Mises stress distribution within eight selected microcubes with different porosity that have been subjected to a uniaxial compression strain of 0.5%. (For interpretation of the references to color in this figure, the reader is referred to the web version of this article.)

32.88% (Table 3). Fig. 7 shows the von Mises stress distribution of 8 selected microcubes that have been subjected to a uniaxial compression strain of 0.5%, and Fig. 8 shows the uniaxial compression stress-strain curves obtained by FEM simulation for all 15 microcubes, including 14 porous microcubes and one with 0% porosity. For consistency, the nominal engineering strain is defined as the ratio of the displacement of the top rigid platen to initial height of the microcube, and the nominal stress is defined as the reaction force of the top rigid platen divided by the total cross-sectional area (i.e., including both the area occupied by the solid metal as well as the area of pores) of the cube. Noticeably, these microcubes are considered as a composite material with two different phases: a solid phase and an air phase. The properties of the solid phase is taken as  $E_s=207$  GPa,  $Y_s=982$  MPa, and  $\nu=0.3$ . For the air phase, the pores inside the microcubes, the mechanical parameters are all taken as 0. As shown in Fig. 7, the von Mises stress is nonuniform within the microcube owing to the presence of irregular voids. At a 0.5% compression strain, the blue regions indicate elastic zones, while the red regions imply the yielded zones. Most red regions take place around the pores due to stress concentra-

tion around the irregular pores. In Fig. 8, the curve with 0% porosity represents the stress-strain behavior of the pore-free ferrous alloy. With increasing porosity, the stress-strain curve is getting lower, the Young's modulus, yield strength, and the yield strain all becomes smaller. After yielding, the porous material behaves perfectly plastic, which is the assumed material behavior.

The FEM simulation results also summarized in Table 3 and also plotted in Fig. 9. Both the Young's modulus and yield strength of the porous wall decrease nonlinearly with increasing porosity. These data are fitted by two equations that can describe the dependence of the Young's modulus and yield strength upon porosity:

$$\frac{E}{E_s} = \left(1 - \frac{\phi}{0.847}\right)^{2.31} \tag{6}$$

$$\frac{Y}{Y_s} = \left(1 - \frac{\phi}{0.847}\right)^{4.05} \tag{7}$$

where  $E$  and  $Y$  are the Young's modulus and yield strength of the porous wall, respectively;  $\phi$  is the volumetric porosity, and the range of

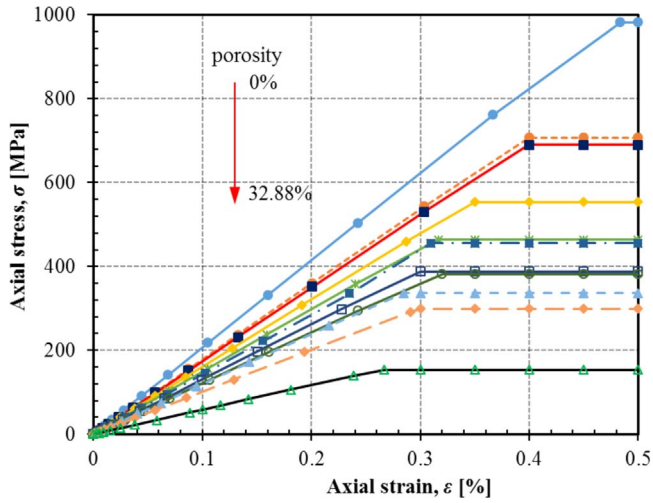


**Fig. 8.** Uniaxial stress-strain curves for all simulated microcubes with porosities ranging from 0% to 32.88% (the red arrow indicates the direction of increasing porosity). (For interpretation of the references to color in this figure legend, the reader is referred to the web version of this article.)

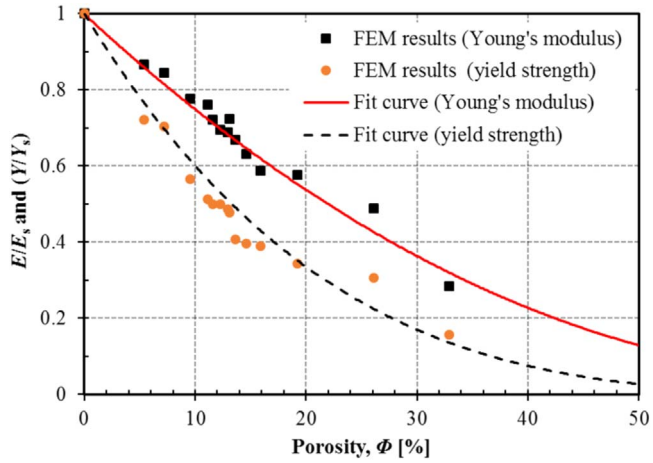


**Fig. 9.** Dependence of Young's modulus and yield strength on porosity, including FEM simulated results and fitted curve.

$0 \leq \Phi \leq 50\%$  is considered in this study. The coefficients of determination (i.e.,  $R^2$ ) for the two fitting equations are 0.9745 and 0.9621, respectively. The parameters in these two equations should not be interpreted as the percolation exponent or threshold, respectively. When  $\Phi$  is 30%, the porous wall loses its stiffness by ~60% and yield strength by ~80%. When  $\Phi$  is greater than 50%, the material almost loses its entire stiffness (i.e., by ~90%) and load-carrying capability (i.e., by ~95%), so the porosity should be controlled accordingly to warrant the desired mechanical properties of individual MHS and MHS-based foam materials.

### 3.5. Comparison with published data

An extensive review of the pertinent literature has found a series of equations that were proposed to account for the dependence of elasticity on porosity for porous metallic materials, and five most relevant ones are summarized as follows:

$$\frac{E}{E_s} = (1 - \phi) \tag{8}$$

$$\frac{E}{E_s} = (1 - \phi)^2 \tag{9}$$

$$\frac{E}{E_s} = \left(1 - \frac{\phi}{0.652}\right)^{2.23} \tag{10}$$

$$\frac{E}{E_s} = \left(1 - \frac{\phi}{0.5}\right)^{2.5} \tag{11}$$

$$\frac{E}{E_s} = (1 - \phi)^3 \tag{12}$$

where  $E$ ,  $E_s$ ,  $Y$ ,  $Y_s$ , and  $\Phi$  have been defined previously. Eq. (8) is proposed to obtain the elastic modulus of a binary composite material based on the volumetric fraction (or porosity if one of the two phases is void) using the so-called “rules of mixtures” [37]. Eq. (9) is the differential and dilute results of the Coble-Kingery correction to describe the elastic modulus of a porous material with spherical pores [38]. Meanwhile, it is also applicable to open-cell materials. Eq. (10) is an empirical correlation based on computational results that can be used to estimate the elastic modulus of a porous material consisting of overlapping solid spheres with inter-sphere porosity [16]. Eq. (11) is used to measure and predict the elastic modulus of the porous 8360 cast steel [39]. Eq. (12) is derived by Maiti et al. for materials containing self-closed pores [40]. It is clearly seen that each of the above equations can be re-written as a unified format:

$$\frac{E}{E_s} = \left(1 - \frac{\phi}{\phi_0}\right)^n \tag{13}$$

where the constant  $\Phi_0$  may correspond to a characteristic porosity of the porous material, and the constant  $n$  may be related to the pore characteristics, such as pore size and its distribution, pore shape, and pore spacing and location distribution, among others. Furthermore,  $\Phi_0$  should be combined with the characteristics of elastic modulus and yield strength comprehensively instead of interpreted as a threshold.

Fig. 10a compares the newly derived model obtained in this study with those previously developed equations for porous materials with a porosity ranging from 0% to 50%. The empirical formula derived in this paper lies in between the Coble-Kingery correction function (i.e., Eq. (9)) and the Maiti et al. equation (i.e., Eq. (12)) for materials with self-closed pores, but is much more closer to the later. This observation may imply that the porous MHS wall material contains both self-closed and open pores, and the percentage of the former is greater than that of the latter. As discussed earlier, the XCT-derived microstructure images do support this kind of pore morphology: most pores within the wall are self-closed, while some pores on the edge of the wall are open.

Khori et al. [41] have studied a porous wall material made of stainless steel, which has a randomly-packed hollow sphere (RHS) configuration. It was processed by spark plasma at high temperatures. Their experimental data of Young's modulus and porosity are here compared with the results of different methods in Fig. 10a. For porosities  $\Phi < 0.4$ , the newly developed equation has an excellent agreement with the experimental data. When  $\Phi > 0.4$ , a very small difference exist between them. In general, the new formula developed in this paper matches the experimental data very well.

There are much fewer reported studies on the yield strength of porous ferrous alloy or other foam material, one of which proposed the following formula for an open-cell foam material – [42]:

$$\frac{Y}{Y_s} = 0.3(1 - \phi)^{\frac{3}{2}} \tag{14}$$

The volumetric porosity,  $\Phi$ , is always greater than 0.37 in this equation. In Fig. 10b, the yield strength-porosity relationship obtained in this study is slightly lower than that calculated by Eq. (14). The difference may be caused by the different pore morphology: Eq. (14) was developed for open-pore materials, while Eq. (7) developed in this study is derived from a material with mostly self-closed pores. In addition, for the porous MHS wall, when  $\Phi > 0.37$ , the porous wall can hardly possess load-carrying capability, and Eq. (14) may overestimate

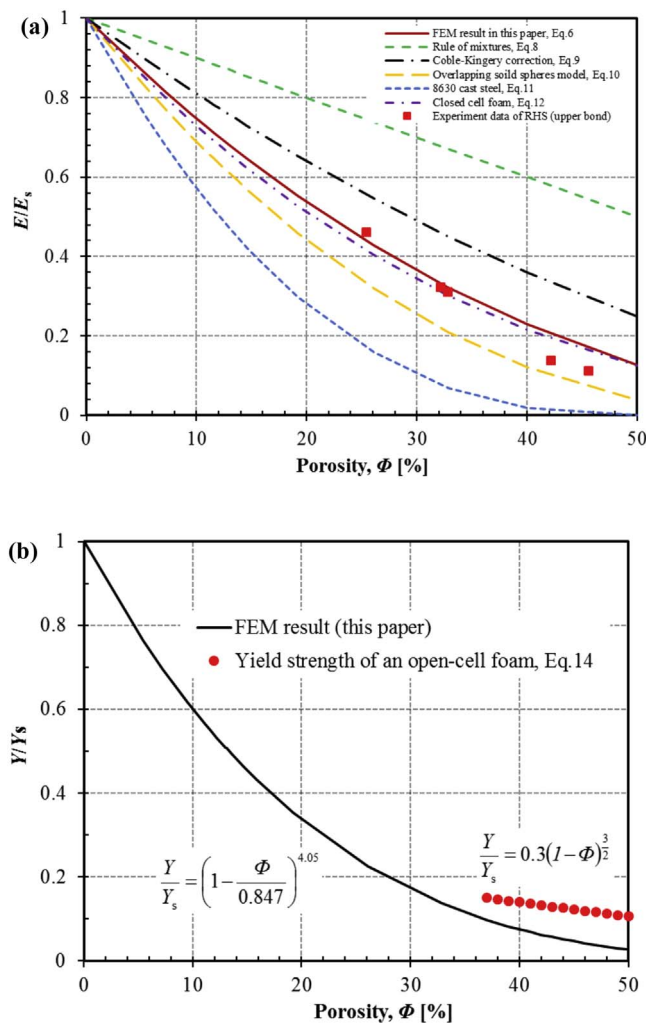


Fig. 10. Comparison of the new formula developed in this study with prior results: (a) Young's modulus; (b) yield strength.

the yield strength by assuming unrealistic pore size or pore morphology.

#### 4. Conclusions

This paper presents an integrated experimental and computational study on the effects of microporosity on the elasticity and yielding of the porous MHS thin wall. Based on the above analyses of results and discussion, the following conclusions can be drawn:

- The mechanical properties of the nonporous MHS wall material were probed by nanoindentation, giving a Young's modulus of 207 GPa, hardness of 2.95 GPa, and yield strength of 982 MPa;
- The MHS thin wall is highly porous with typical pore sizes ranging from a few micrometers to 15  $\mu\text{m}$  and microporosities of up to 42%.
- The Young's modulus and yield strength of the porous MHS thin wall both decrease nonlinearly with porosity, and their dependence on porosity can be described by two power functions of similar format, but with different power values (i.e., a power of 2.31 for the elastic modulus, while a power of 4.05 for yield strength).
- The new FEM-derived mechanical property – microporosity relationships agree much better with experimental data than other simplified theoretical and empirical correlations.
- The morphology of the pores in the MHS thin wall is very complex, and both open and self-closed pores co-exist.

- The integrated approach developed in this study is based on the real microstructure of the porous MHS thin wall, and hence provide a more accurate correlation between the mechanical properties and porosity.

#### Acknowledgments

The first author (J.S.) was supported by a Visiting Scholarship Award from the China Scholarship Council. The work was also partially supported by the corresponding author (G.Z.)'s startup fund provided by the Department of Civil and Environmental Engineering at the University of Massachusetts Amherst, including the acquisition of the Keysight G200 nanoindenter.

#### References

- [1] A. Rabiei, L.J. Vendra, A comparison of composite metal foam's properties and other comparable metal foams, *Mater. Lett.* 63 (2009) 533–536. <http://dx.doi.org/10.1016/j.matlet.2008.11.002>.
- [2] W. Sanders, L. Gibson, Mechanics of BCC and FCC hollow-sphere foams, *Mater. Sci. Eng. A* 352 (2003) 150–161. [http://dx.doi.org/10.1016/S0921-5093\(02\)00890-0](http://dx.doi.org/10.1016/S0921-5093(02)00890-0).
- [3] O. Caty, E. Maire, R. Bouchet, Fatigue of metal hollow spheres structures, *Adv. Eng. Mater.* 10 (2008) 179–184. <http://dx.doi.org/10.1002/adem.200700265>.
- [4] T.J. Lim, B. Smith, D.L. McDowell, Behavior of a random hollow sphere metal foam, *Acta Mater.* 50 (2002) 2867–2879. [http://dx.doi.org/10.1016/S1359-6454\(02\)00111-8](http://dx.doi.org/10.1016/S1359-6454(02)00111-8).
- [5] A. Taşdemirci, Ç. Ergöncü, M. Güden, Split Hopkinson pressure bar multiple reloading and modeling of a 316 L stainless steel metallic hollow sphere structure, *Int. J. Impact Eng.* 37 (2010) 250–259. <http://dx.doi.org/10.1016/j.ijimpeng.2009.06.010>.
- [6] A. Fallet, P. Lhuissier, L. Salvo, Y. Bréchet, Mechanical behaviour of metallic hollow spheres foam, *Adv. Eng. Mater.* 10 (2008) 858–862. <http://dx.doi.org/10.1002/adem.200800094>.
- [7] Z.Y. Gao, T.X. Yu, H. Zhao, Mechanical behavior of metallic hollow sphere materials: experimental study, *J. Aerosp. Eng.* 21 (2008) 206–216. [http://dx.doi.org/10.1061/\(ASCE\)0893-1321\(2008\)21:4\(206\)](http://dx.doi.org/10.1061/(ASCE)0893-1321(2008)21:4(206)).
- [8] O. Caty, E. Maire, S. Youssef, R. Bouchet, Modeling the properties of closed-cell cellular materials from tomography images using finite shell elements, *Acta Mater.* 56 (2008) 5524–5534. <http://dx.doi.org/10.1016/j.actamat.2008.07.023>.
- [9] I. Shufrin, E. Pasternak, A.V. Dyskin, Negative Poisson's ratio in hollow sphere materials, *Int. J. Solids Struct.* 54 (2015) 192–214. <http://dx.doi.org/10.1016/j.jisolsolstr.2014.10.014>.
- [10] O. Friedl, C. Motz, H. Peterlik, S. Puchegger, N. Reger, R. Pippan, Experimental investigation of mechanical properties of metallic hollow sphere structures, *Metall. Mater. Trans. B* 39 (2008) 135–146. <http://dx.doi.org/10.1007/s11663-007-9098-2>.
- [11] Z. Hashin, Analysis of composite-materials – a survey, *J. Appl. Mech. – Trans. ASME* 50 (1983) 481–505. <http://dx.doi.org/10.1115/1.3167081>.
- [12] J. Aboudi, *Mechanics of composite materials: a unified micromechanical approach*, *Stud. Appl. Mech.* 29 (1991) 328.
- [13] R.M. Christensen, *Mechanics of Composite Materials*, Dover, Mineola, New York, 1979, pp. 31–72.
- [14] R.W. Rice, Evaluation and extension of physical property-porosity models based on minimum solid area, *J. Mater. Sci.* 31 (1996) 102–118. <http://dx.doi.org/10.1007/BF00355133>.
- [15] R.W. Rice, Comparison of physical property-porosity behaviour with minimum solid area models, *J. Mater. Sci.* 31 (1996) 1509–1528. <http://dx.doi.org/10.1007/BF00357860>.
- [16] A. Roberts, E. Garboczi, Elastic properties of model porous ceramics, *J. Am. Ceram. Soc.* 83 (2000) 3041–3048. <http://dx.doi.org/10.1111/j.1151-2916.2000.tb01680.x>.
- [17] J.G. Sanjayam, A. Nazari, H. Pouraliakbar, FEA modelling of fracture toughness of steel fibre-reinforced geopolymer composites, *Mater. Des.* 76 (2015) 215–222. <http://dx.doi.org/10.1016/j.matdes.2015.03.029>.
- [18] E. Ranjbari, H. Pouraliakbar, A.H. Kokabi, Finite element simulation of carbide precipitation in austenitic stainless steel 304, *Int. J. Mech. Appl.* 2 (2012) 117–123. <http://dx.doi.org/10.5923/j.mechanics.20120206.03>.
- [19] W.C. Oliver, G.M. Pharr, An improved technique for determining hardness and elastic modulus using load and displacement sensing indentation experiments, *J. Mater. Res.* 7 (1992) 1564–1583. <http://dx.doi.org/10.1557/JMR.1992.1564>.
- [20] G.M. Pharr, W.C. Oliver, F.R. Brotzen, On the generality of the relationship among contact stiffness, contact area, and elastic-modulus during indentation, *J. Mater. Res.* 7 (1992) 613–617. <http://dx.doi.org/10.1557/JMR.1992.0613>.
- [21] G. Zhang, Z. Wei, R. Ferrell, Elastic modulus and hardness of muscovite and rectorite determined by nanoindentation, *Appl. Clay Sci.* 43 (2009) 271–281. <http://dx.doi.org/10.1016/j.clay.2008.08.010>.
- [22] A.C. Kak, M. Slaney, *Principles of Computerized Tomographic Imaging*, IEEE, New York, 1988.
- [23] B.A. Dowd, G.H. Campbell, R.B. Marr, V.V. Nagarkar, S.V. Tipnis, L. Axe, D.P. Siddons, Developments in synchrotron x-ray computed microtomography at

- the National Synchrotron Light Source, Proc. SPIE 3772 (1999) 224–236. <http://dx.doi.org/10.1117/12.363725>.
- [24] D. Gürsoy, F. De Carlo, X. Xiao, C. Jacobsen, TomoPy: a framework for the analysis of synchrotron tomographic data, *J. Synchrotron Radiat.* 21 (2014) 1188–1193. <http://dx.doi.org/10.1107/S1600577514013939>.
- [25] S. van der Walt, J.L. Schönberger, J. Nunez-Iglesias, F. Boulogne, J.D. Warner, N. Yager, E. Gouillart, T. Yu, Scikit-image: image processing in Python, *PeerJ* 2 (2014) e453. <http://dx.doi.org/10.7717/peerj.453>.
- [26] R. Agrawal, B. Peng, E.E. Gdoutos, H.D. Espinosa, Elasticity size effects in ZnO nanowires – a combined experimental-computational approach, *Nano Lett.* 8 (2008) 3668–3674. <http://dx.doi.org/10.1021/nl801724b>.
- [27] Y. Zheng, Y. Zhao, H. Ye, H. Zhang, Size-dependent elastic moduli and vibrational properties of fivefold twinned copper nanowires, *Nanotechnology* 25 (2014) 315701. <http://dx.doi.org/10.1088/0957-4484/25/31/315701>.
- [28] H. Yao, G. Yun, W. Fan, Size effect of the elastic modulus of rectangular nanobeams: surface elasticity effect, *Chin. Phys. B* 22 (2013) 106201. <http://dx.doi.org/10.1088/1674-1056/22/10/106201>.
- [29] T. Takahashi, J. Burghaus, D. Music, R. Dronskowski, J.M. Schneider, Elastic properties of  $\gamma'$ -Fe<sub>4</sub>N probed by nanoindentation and ab initio calculation, *Acta Mater.* 60 (2012) 2054–2060. <http://dx.doi.org/10.1016/j.actamat.2011.12.051>.
- [30] C. Tromas, J.C. Stinville, C. Templier, P. Villechaise, Hardness and elastic modulus gradients in plasma-nitrided 316L polycrystalline stainless steel investigated by nanoindentation tomography, *Acta Mater.* 60 (2012) 1965–1973. <http://dx.doi.org/10.1016/j.actamat.2011.12.012>.
- [31] W.D. Nix, H. Gao, Indentation size effects in crystalline materials: a law for strain gradient plasticity, *J. Mech. Phys. Solids* 46 (1998) 411–425. [http://dx.doi.org/10.1016/S0022-5096\(97\)00086-0](http://dx.doi.org/10.1016/S0022-5096(97)00086-0).
- [32] D. Tabor, The physical meaning of indentation and scratch hardness, *Br. J. Appl. Phys.* 7 (1956) 159. <http://dx.doi.org/10.1088/0508-3443/7/5/301>.
- [33] J. Ballarre, E. Jimenez-Pique, M. Anglada, S.A. Pellice, A.L. Cavalieri, Mechanical characterization of nano-reinforced silica based sol–gel hybrid coatings on AISI 316L stainless steel using nanoindentation techniques, *Surf. Coat. Technol.* 203 (2009) 3325–3331. <http://dx.doi.org/10.1016/j.surfcoat.2009.04.014>.
- [34] H. Kim, C. Kim, F. Barlat, E. Pavlina, M.-G. Lee, Nonlinear elastic behaviors of low and high strength steels in unloading and reloading, *Mater. Sci. Eng. A* 562 (2013) 161–171. <http://dx.doi.org/10.1016/j.msea.2012.11.020>.
- [35] G. Cheng, F. Zhang, A. Ruimi, D.P. Field, X. Sun, Quantifying the effects of tempering on individual phase properties of DP980 steel with nanoindentation, *Mater. Sci. Eng. A* 667 (2016) 240–249. <http://dx.doi.org/10.1016/j.msea.2016.05.011>.
- [36] A. Kumar, B. Bhushan, Nanomechanical, nanotribological and macrotribological characterization of hard coatings and surface treatment of H-13 steel, *Tribol. Int.* 81 (2015) 149–158. <http://dx.doi.org/10.1016/j.triboint.2014.08.010>.
- [37] T. Sumitomo, C.H. Cáceres, M. Veidt, The elastic modulus of cast Mg–Al–Zn alloys, *J. Light Met.* 2 (2002) 49–56. [http://dx.doi.org/10.1016/S1471-5317\(02\)00013-5](http://dx.doi.org/10.1016/S1471-5317(02)00013-5).
- [38] R.L. Coble, W.D. Kingery, Effect of porosity on physical properties of sintered alumina, *J. Am. Ceram. Soc.* 39 (1956) 377–385. <http://dx.doi.org/10.1111/j.1151-2916.1956.tb15608.x>.
- [39] R. Hardin, C. Beckermann, Simulation of the mechanical performance of cast steel with porosity: static properties, in: Proceedings of the 60th SFSA Technical and Operating Conference, Paper No. 4.3, Steel Founders' Society of America, Chicago, IL, 2006.
- [40] S.K. Maiti, L.J. Gibson, M.F. Ashby, Deformation and energy absorption diagrams for cellular solids, *Acta Metall.* 32 (1984) 1963–1975. [http://dx.doi.org/10.1016/0001-6160\(84\)90177-9](http://dx.doi.org/10.1016/0001-6160(84)90177-9).
- [41] K.A. Khor, L.G. Yu, O. Andersen, G. Stephani, Effect of spark plasma sintering (SPS) on the microstructure and mechanical properties of randomly packed hollow sphere (RHS) cell wall, *Mater. Sci. Eng. A* 356 (2003) 130–135. [http://dx.doi.org/10.1016/S0921-5093\(03\)00111-4](http://dx.doi.org/10.1016/S0921-5093(03)00111-4).
- [42] L.J. Gibson, M.F. Ashby, The mechanics of three-dimensional cellular materials, *Proc. R. Soc. Lond. A Math. Phys. Eng. Sci.* 382 (1982). <http://dx.doi.org/10.1098/rspa.1982.0088>.